High-contrast imager for Complex Aperture Telescopes (HiCAT). 4. Status and wavefront control development

Lucie Leboulleux[a][b][c], Mamadou N'Diaye[a], A J Eldorado Riggs[d], Sylvain Egron[a][b][c], Johan Mazoyer[a], Laurent Pueyo[a], Elodie Choquet[e][f], Marshall D. Perrin[a], Jeremy Kasdin[d], Jean-François Sauvage[b][c], Thierry Fusco[b][c], and Rémi Soummer[a]

[a] Space Telescope Science Institute, 3700 San Martin Drive, Baltimore, MD 21218, USA
[b] Aix Marseille Université, CNRS, LAM (Laboratoire d'Astrophysique de Marseille) UMR 7326, 13388, Marseille, France
[c] Office National d'Etudes et de Recherches Aérospatiales, 29 Avenue de la Division Leclerc, 92320 Châtillon, France
[d] Princeton University, Department of Mechanical and Aerospace Engineering, Engineering Quadrangle, Princeton, NJ 08544, USA
[e] Jet Propulsion Laboratory, California Institute of Technology, 4800 Oak Grove Drive, MS 169-506, Pasadena, CA 91109, USA
[f] Hubble Fellow

ABSTRACT

Segmented telescopes are a possible approach to enable large-aperture space telescopes for the direct imaging and spectroscopy of habitable worlds. However, the increased complexity of their aperture geometry, due to their central obstruction, support structures and segment gaps, makes high-contrast imaging very challenging.

The High-contrast imager for Complex Aperture Telescopes (HiCAT) was designed to study and develop solutions for such telescope pupils using wavefront control and starlight suppression. The testbed design has the flexibility to enable studies with increasing complexity for telescope aperture geometries starting with off-axis telescopes, then on-axis telescopes with central obstruction and support structures (e.g. the Wide Field Infrared Survey Telescope [WFIRST]), up to on-axis segmented telescopes e.g. including various concepts for a Large UV, Optical, IR telescope (LUVOIR), such as the High Definition Space Telescope (HDST). We completed optical alignment in the summer of 2014 and a first deformable mirror was successfully integrated in the testbed, with a total wavefront error of 13nm RMS over a 18mm diameter circular pupil in open loop. HiCAT will also be provided with a segmented mirror conjugated with a shaped pupil representing the HDST configuration, to directly study wavefront control in the presence of segment gaps, central obstruction and spider.

We recently applied a focal plane wavefront control method combined with a classical Lyot coronagraph on HiCAT, and we found limitations on contrast performance due to vibration effect. In this communication, we analyze this instability and study its impact on the performance of wavefront control algorithms. We present our Speckle Nulling code to control and correct for wavefront errors both in simulation mode and on testbed mode. This routine is first tested in simulation mode without instability to validate our code. We then add simulated vibrations to study the degradation of contrast performance in the presence of these effects.

Keywords: exoplanets, high-contrast imaging, wavefront sensing, wavefront control, Speckle Nulling, vibration analysis

1. INTRODUCTION

The next generation of space telescopes for direct imaging and spectroscopy of exoplanets includes telescopes with a monolithic mirror, such as the Wide Field Infrared Survey Telescope (WFIRST),[1] and Large Ultra-Violet

---

Further author information, send correspondence to Lucie Leboulleux: E-mail: leboulleux@stsci.edu, Telephone: 1 410 338 2881

Optical Infrared (LUVOIR) telescopes with segmented primary mirror, like ATLAST[2,3] or HDST.[4] Because of the complexity of their pupils, high-contrast imaging becomes more challenging, including starlight suppression with coronagraphy and wavefront sensing and wavefront control for contrast stability in the presence of vibrations.

The High-contrast imager for Complex Aperture Telescopes (HiCAT) testbed has been developed to enable studies on starlight suppression, wavefront sensing (WFS), and wavefront control (WFC) for such unfriendly pupils. New coronagraph designs for any kind of aperture that are based on the Apodized Pupil Lyot Coronagraph (APLC)[5,6] are currently developed on simulation and will then be implemented on the testbed. Furthermore, new high-contrast methods will be implemented and tested, such as pupil remapping techniques (e.g. Active Control of Aperture Discontinuities [ACAD][7–9]) that use two deformable mirrors (DMs) to convert complex pupils into friendly apertures for coronagraphy.

In previous papers, we presented the overall goals and design of HiCAT[10,11] and described its assembly and integration including the installation and first tests with single Boston Micromachines deformable mirror (DM).[12]

In this communication, we report on progress and challenges since then. In particular we describe the detection and analysis of instability that prevents us from implementing high-contrast imaging codes on HiCAT. From these studies, we derive a new DM mount design and the implementation of a Speckle Nulling code in simulation, without and with instability.

In Section 2, we present the main features of our testbed and our first wavefront control tests. We show that the preliminary results did not reach the desired contrast levels because of the instability issues that were detected during our experiments. In Section 3, we analyze the point spread function (PSF) motion that was observed on the testbed and we derive conclusions on the instability issues. Finally, in Section 4, we present the results of our simulations on wavefront control using a single DM and a classical Lyot coronagraph, including instability effects.

2. HICAT TESTBED IMPLEMENTATION AND STATUS

2.1 Optical and opto-mechanical designs

The detailed optical design of the testbed was presented in N'Diaye et al.[10] and it will at the end simulate a complex aperture telescope on which the starlight will be suppressed thanks to an APLC and wavefront control, using two DMs. The design goal was to minimize amplitude-induced errors due to Talbot effects. In addition, the access to several pupil and focal planes enables the correction of phase errors induced by aperture diffraction. As shown in Fig. 1, the HiCAT testbed is provided with a starlight suppression system, based on the APLC architecture. This includes a reflective apodizer,[13] a reflective Focal Plane Mask (FPM), which currently has a 334 micrometer size hole at its center, and a Lyot Stop. Both the Lyot Stop and the FPM are motorized and can be controlled from a computer. The final design of the apodizer is still under development as part of our ongoing coronagraph optimization studies,[6] so it is currently replaced with a high quality flat mirror and the full starlight suppression system is currently equivalent to a Lyot coronagraph.
Two DMs (Boston kilo-DM) enable wavefront sensing and control studies on HiCAT. The first one has been set up in a pupil plane in 2014-2015 and allows first studies to be driven.[12] The second one, out of pupil plane, is not installed yet and is currently replaced by a high quality flat mirror.
Furthermore, since HiCAT should be able to simulate a telescope with a complex geometry pupil, it can be featured with a pupil mask similar to the WFIRST pupil, including the spider and the central obstruction. It will also be provided with a segmented mirror (SM), conjugated with the previous complex pupil to simulate an ATLAST/HDST-like primary mirror. This mirror is an Iris-AO SM with 36 segments.
At the very end of the testbed, a beam splitter sends the beam to two cameras, CamF and CamP, respectively installed at a focal plane and at a pupil plane.

The testbed is fully aligned with an excellent wavefront quality of 13nm RMS over a 18mm diameter circular pupil[11] and now includes all the convergent and flat mirrors, the beam launcher, the pupil mask, the first DM (DM1) which is set in a pupil plane, the FPM, the Lyot Stop, and the two cameras. To reduce the stray light, it also has an enclosure, several black screens and laser beam dumps.
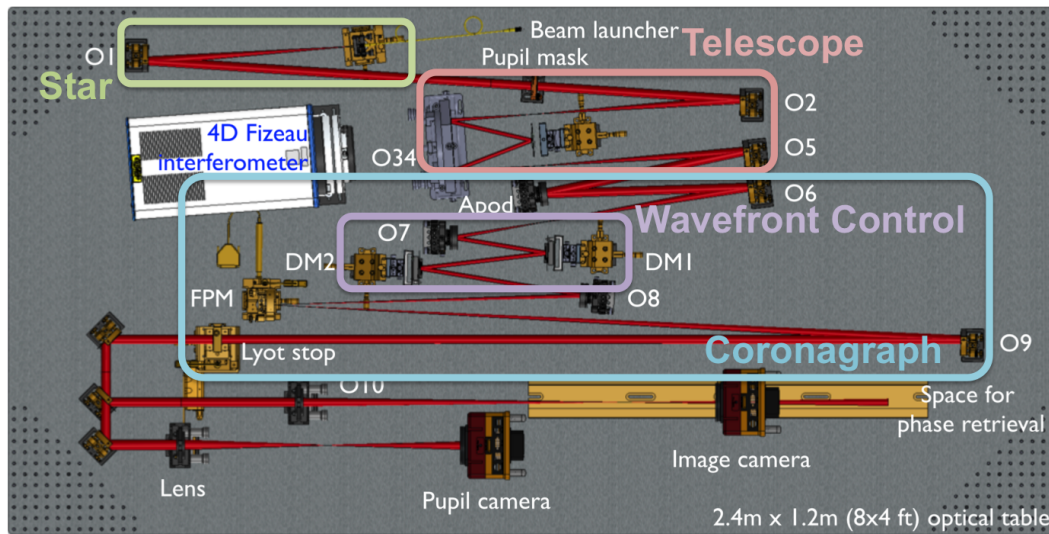
Figure 1. HiCAT testbed design done with the software Solidworks, the beam is exported from Zemax. The telescope is simulated by a pupil mask, the segmented mirror and off-axis parabolas. The segmented mirror is conjugated with the pupil mask to form a segmented pupil with central obstruction and spider struts. The off-axis parabolas set the telescope aperture. The wavefront control is done with two deformable mirrors. The coronagraph is composed of an apodizer, a focal plane mask and a Lyot stop.

It will also have to be upgraded with the WFIRST-like pupil mask, the SM conjugated with the previous complex pupil to simulate a ATLAST/HDST-like primary mirror, the apodizer that is currently being designed and a second Boston kilo-DM, out of pupil plane.

2.2 Wavefront sensing and wavefront control implementation

In 2015, a first Speckle Nulling code was implemented on the HiCAT testbed, using DM1. It enabled the suppression of a speckle in our final image. For more details about this first implementation, please see N'Diaye et al. 2015.[12]

After this first step, we tested a Focal Plane Wavefront Control (FPWC) code[14] but we did not manage to produce a dark hole with the expected contrast because of some Point Spread Function (PSF) drifts between the different exposures.

3. INSTABILITY ANALYSIS

In this section, we present our instability analysis and introduce a new DM mount design, that should be an important improvement compared to the current one.

3.1 PSF motion analysis

The idea here is to characterize the motion effect on recorded videos and, depending on the kind of motion or shape changing we observe, to find both the source of the vibration and its support on the testbed. For example, the motor driver could be the origin of the vibration, but it does not have an real direct influence on the beam, unless an optical component is loose. In the following sections, we present our main tests and the derived conclusions.

The criteria to characterize the motion are:
- the amplitude of the motion around an average position as a function of the time
- the direction of the motion (the motion could follow only the Y-axis, for example)
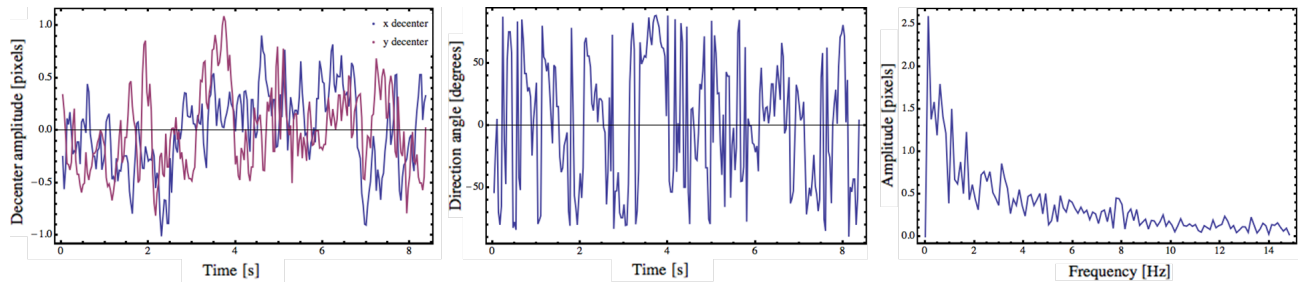- the spectrum of the motion.

Figure 2. Analysis of the PSF motion when HiCAT is at rest (all the hardware is on, the enclosure is closed and the camera is at the end of the testbed). Left: distance in pixels of the PSF from the mean position as a function of time. Center: direction of the motion on the detector as a function of time. No privileged direction appears here. Right: Spectrum of the motion. The motion is obviously a low frequency movement, there is no high frequency peak.

Our tests were done using a Thorlabs CMOS camera, that can take monochrome videos at a frame rate from 25 fps to 250 fps with a 1280 x 1024 pixel detector, where each pixel is a 5.20 μm square. In addition, the small size of the camera (48.6 mm × 44 mm × 25.7 mm) facilitates access to the different planes of study.

3.1.1 HiCAT at rest

As a reference comparison for the following tests, if HiCAT is at rest, so in normal running conditions (hardwares are on and the enclosure is closed), we obtain the results shown in Fig. 2. No main direction of motion could be obtained from the video analysis and only frequencies below 2 Hz seem to appear. Indeed, above 2 Hz, we cannot see any specific peak in the spectrum.

Furthermore, we realigned all the frames from a video, where the coronagraph is set, and we noticed after realignment that the PSF was not moving anymore, except that the shape of the core of the coronagraphic PSF was modified with time. This observation made us conclude that there is at least one optical component moving before the FPM.

3.1.2 Which optical components are most unstable?

To find out which optical component could be responsible for the beam direction to change in the testbed, two sets of tests were done.

First, we set the camera at the end of the testbed, at the focal plane and gently tap every optical component that appears on Fig. 1 except for DM1. The idea here is to check if tapping has an influence on the PSF motion. The three main results from these first tests are given in Fig. 3 and tapping every other optical component has no effect on the PSF instability. For these three optics, so DM2, the apodizer and the Iris AO (actually flat mirrors), we do observe an important change of the amplitude and spectrum of the PSF motion.

As a second set of test, we put successively the camera at each of the five focal planes of the testbed and compare the amplitude of the PSF motion normalized by the value of the focal length until this focal plane, which is equivalent of getting a value of the amplitude of the motion angle of the beam instead of the metric amplitude of the PSF. In theses conditions, the amplitude values can be compared even if the camera is set at different focal planes.
Without a surprise, the further the camera is from the entrance of the testbed, the worse the amplitude is. We mainly observe the most significant difference between the two focal planes situated right before and right after the two DMs and the mirror O8: the average motion values are multiplied by 3.20 between these two successive focal planes. These three optical components, DM1 and DM2 and O8, then become principal suspects.

As a final test, since our two previous tests were never done on DM1 that is too easily damageable, we built a spare mount, similar to DM1 mount, and set it up in the beam path of the testbed to study its stability as well. We can conclude from the results we obtain that tapping this mount has a huge influence on the PSF motion amplitude (the average value of the motion amplitude is multiplied by 4.87), which means that DM1 is unstable too and can also be considered as a suspect of the PSF motion.
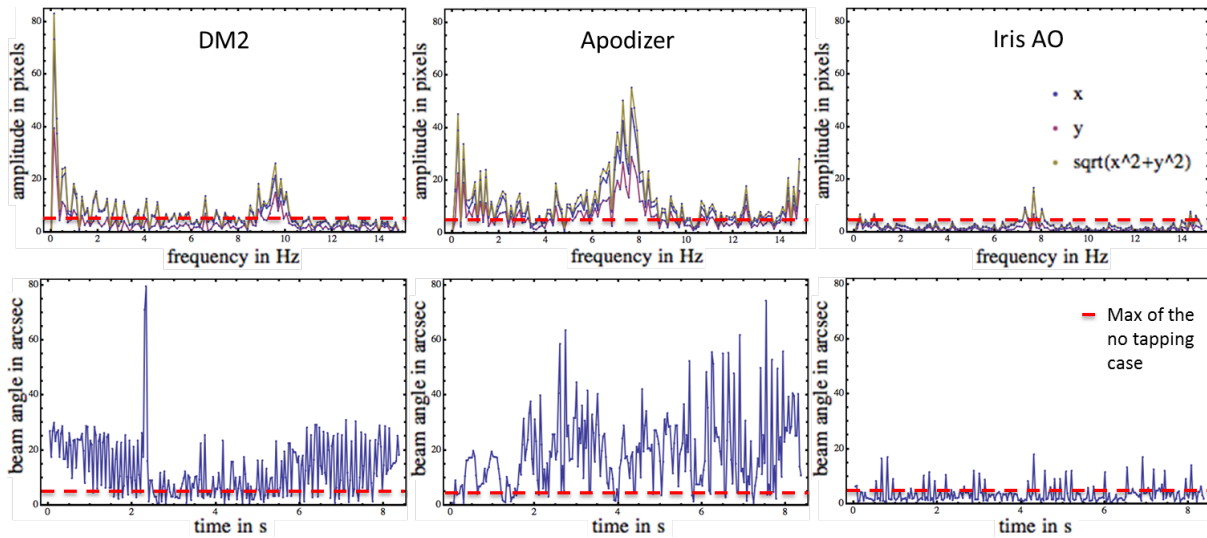
Figure 3. Temporal amplitude (top) and spectra (bottom) of the PSF motion obtained from a video acquisition when tapping three optical components. Left: the flat mirror replacing DM2, middle: the flat mirror replacing the apodizer, right: the flat mirror replacing the Iris-AO segmented mirror. The red lines correspond to the maximum value obtained without tapping.

3.1.3 Which source(s) drive(s) the instability?

This test consists in turning off one by one every possible source of motion in the testbed environment, such as the camera fans, the drivers or the air supply and taking videos at the end of the testbed.

After analysing the different recorded videos, we reached the conclusion that the motor driver and mainly the camera fans were responsible for the PSF motion. For the cameras turned off, the average motion amplitude indeed decreased by a factor of 1.45 and if the motor driver is turned off, it is decreased by a factor of 1.26.

3.1.4 Conclusion on vibration analysis

In conclusion, the motor driver and the camera fans seem responsible for the motion of the PSF and this motion of the sources can be transmitted to the beam train thanks to different possible loose or unstable optics: the two DMs, the flat mirror replacing the SM, and the apodizer.

All these optics are located before the FPM, which makes sense since when the coronagraph is on, the shape of the core of the PSF is changing.

This study still gives a large panel of suspects and careful checking of the assembly and mounting screws for all testbed optomechanics did not result in any improvements in stability. Rather it appears that one or more mount designs themselves are insufficiently stable.

3.2 Mechanical improvement on the DM mount

As we showed in the previous part, DM1 seems to be the most likely source of the vibration effect, which can easily be explained since the current mount is really cantilevered. After this analysis, it was decided to re-design this mount to make it as stable as possible.

The main constraints that have to be respected are the radius of curvature of the goniometer, the beam height (both of them have to correspond to the DM center) and the mount stability. We finally reach the global design presented in Fig. 4, where all the components are set above each other, following a vertical axis that makes the global structure really more stable than the current one.

4. SPECKLE NULLING SIMULATION TESTS

To study the instability phenomenon, we decided to focus on a well-known procedure: the Speckle Nulling method.
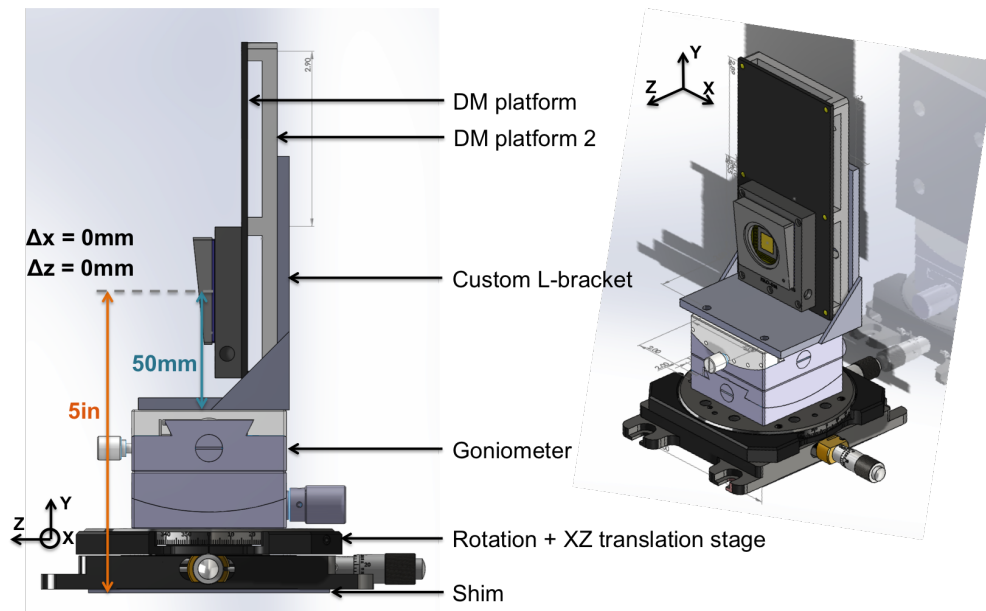
Figure 4. Solidworks design of the mount. Both the center of curvature of the goniometer and the beam height have an origin that corresponds to the DM center. The components are set one above each other, which guarantees better stability than the current cantilevered mount design.

Since Brown and Burrows[15] set the typical requirements in term of contrast for exoplanet detection, the theoretical feasibility of starlight subtraction in a so-called dark hole thanks to a DM has been proven.[16] This approach has been simplified with linearization of the equations to become the Speckle Nulling algorithm which has already several times been experimentally tested and has proven its efficiency and its robustness in broadband light.[17, 18] A first generalization of this method (Speckle Field Nulling), which is based on minimization of the speckle energy in all over the dark hole thanks to a Fast-Fourier-Transform-based (FFT) algorithm, has been developed.[19] In opposition to these estimation-free approaches, model-based techniques are developed and implemented. They separate estimation and control for a faster correction, such as the Self-Coherent Camera (SCC)[20] and the COronagraphic Focal-plane waveFront Estimation for Exoplanet detection (COFFEE)[21] for the estimation, or the Electric Field Conjugation (EFC)[14, 22] and the Stroke Minimization,[23] including even multiple DMs to enable symmetric correction in the dark hole (both amplitude and phase aberration correction).

In this section, we describe in the first part the Speckle Nulling code that is applied in simulation mode in the case of a circular aperture and the results we obtain. In the second part, we add random tip-tilt vibrations in the pupil plane of our simulated system and study the influence of this perturbation on the results.

4.1 Simulation without perturbation

4.1.1 Theory and code

We wrote a code that is split in different parts, to separate the simulation-only sections from the sections common to the simulation mode and to the on-testbed mode. The simulation-only sections are equivalent on the testbed to an image acquisition and therefore contain a simulated Lyot coronagraph similar to the HiCAT configuration. A visual description of the code is given in Fig. 5.

The Speckle Nulling method does not uniformly correct the image in the all dark hole. It typically focuses on the correction of the n brightest speckles of the dark hole. For example, if we only want to correct for one single speckle, the Speckle Nulling method selects the brightest speckle of the dark hole and computes its intensity I and its position (u_x, u_y), according to the center of the PSF.

Since one speckle in the field is equivalent to a sine function of the wavefront surface in the pupil plane, we are looking for an equation of the unknown error phase in the pupil plane such as:
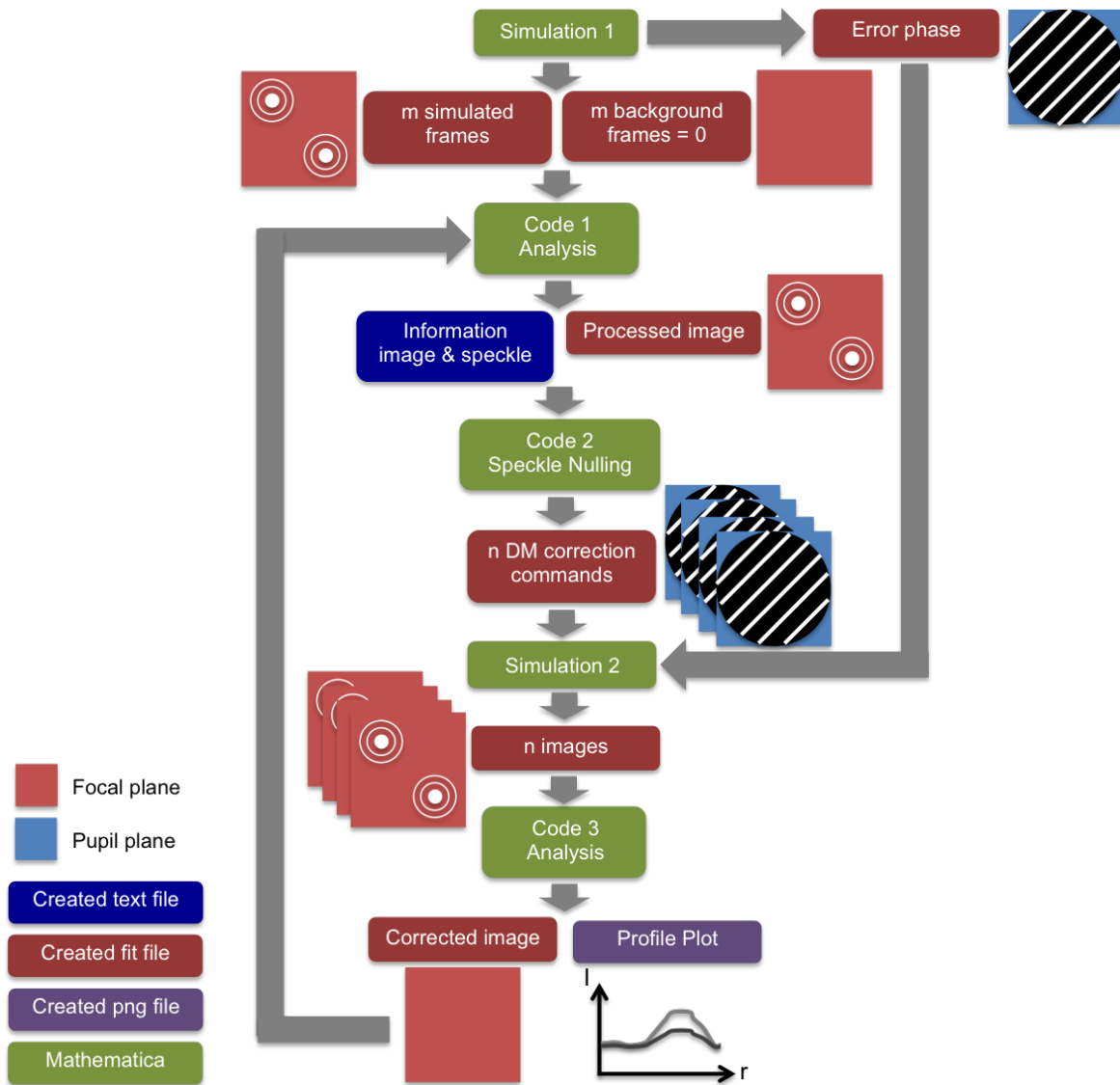
Figure 5. Diagram of our Speckle Nulling code. The code has been written to work in two different modes: with simulated data or experimental images on the testbed. Simulations 1 and 2 are dedicated to the simulation mode only while Codes 1, 2 and 3 are common to the simulation mode and the on-testbed mode. Simulation 1 sets up all the useful input for the rest of the procedure: a fake flat command of the DM, an "unknown" phase error (here: a sine function), background frames and image plane frames obtained with a Lyot coronagraph. Code 1 computes the characteristics of the selected speckle (spatial frequency and amplitude) and takes the average background-subtracted image. Code 2 generates n commands to the DM to probe different spatial phases of the selected speckle. Simulation 2 computes the coronagraphic images in the presence of unknown phase for each of the n commands applied on the DM. Finally, Code 3 analyses the coronagraphic images to determine the phase and the corresponding DM command that allow us to obtain the best correction of the selected speckle.
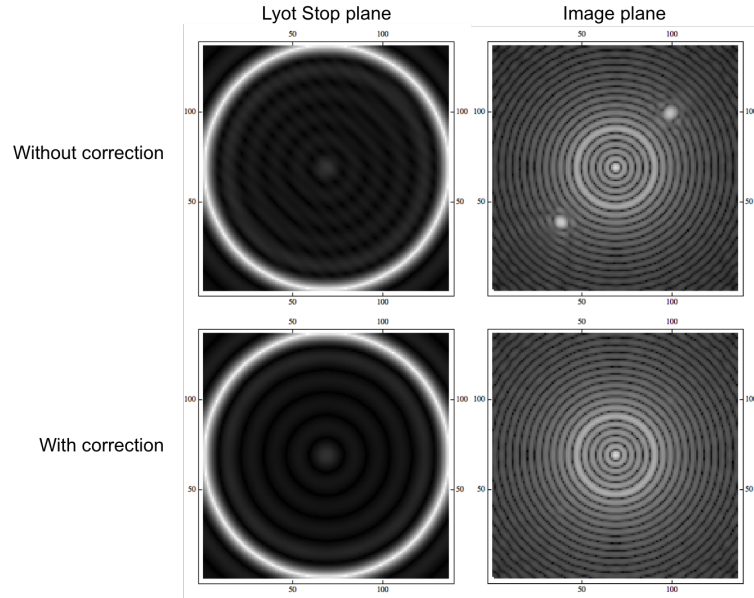
Figure 6. First results obtained with the Speckle Nulling code with simulated images before and after correction of a pair of speckles (top and bottom). Left: Images in the relayed pupil plane of the coronagraph before application of the Lyot stop. Right: Coronagraphic images in the final image plane.

$$\Phi = A \times \sin(\phi_0 + 2\pi \times (f_x x + f_y y)) \tag{1}$$

where A is the amplitude of the sine, ϕ_0 is the origin phase and f_x and f_y are the spatial frequencies of the phase and can easily be computed from the position (u_x, u_y) of the speckle.

Furthermore, to estimate the amplitude of the sine function, we add a calibration step before the correction. A known sine function is applied on the DM surface and we simulate the resulting image in the focal plane behind the coronagraph. This image has two symmetrical speckles, and we can get their intensity. According to this value and the amplitude of the sine command sent to the DM, we have a conversion factor from the DM command to the intensity of the image points.

$$A = C \times A_0 \times \sqrt{\frac{I}{I_0}} \tag{2}$$

where A is the calculated amplitude, A_0 is the amplitude of the calibration sine command, C is the conversion factor, I is the intensity of the speckle that has to be corrected, and I_0 is the intensity of the calibration speckle.

The main problem is finding the spatial phase ϕ_0. As explained in Fig. 5, it is found by testing different possible spatial phases and selecting thanks to an interpolation the one that gives the best results on the corrected image.

4.1.2 Results

We apply the procedure described before on a simulated coronagraph with a Lyot Stop size equal to 0.99 times the pupil size. In this case, since we are working on simulated data, we fix the DM size to 136 actuators, so 4 times larger than our real DM. The error phase is set as shown on Fig. 6 on the top left image and we just have access to the top right image, which is the input of the routine.

We can also observe the results that we obtain after applying the Speckle Nulling code with the best correction to the images. As we can see, the correction was very efficient: in this case, the value of the speckle changed
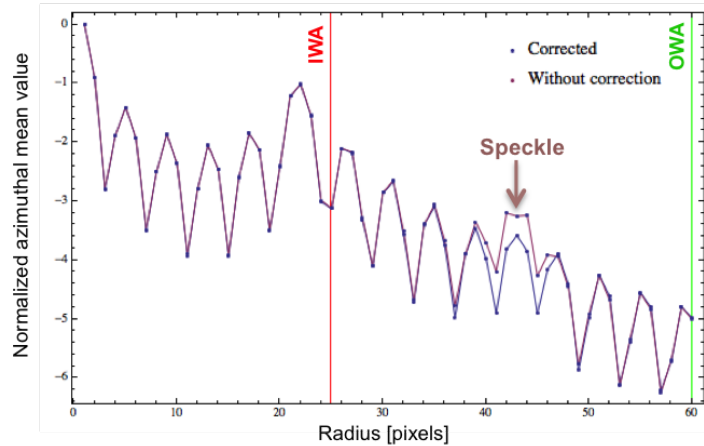
Figure 7. Azimuthal averaged intensity profiles of the coronagraphic images in log scale for the initial image (purple) and the corrected image (blue) that are displayed in Figure 6. The IWA and OWA of the controlled region are represented with vertical lines. The attenuation of the intensity is observed at the speckle location (44 pixels).

from 0.6898 to 0.01247 and on the corrected image, no speckle is visible. If we look at Fig. 7, the absence of speckle on the corrected image also clearly appears.

We also notice that on the simulated resulting phase in the pupil plane, issued from both the error phase and the correction phase, we can observe a non uniform phenomenon. This is due to the Moiré effect (frequency folding), which results from the difference between the spatial frequencies from the error phase and from the correction phase. Let's set the error phase has $(f_x, f_y) = (21, 21)$ as a spatial frequency and the frequency computed thanks to our Speckle Nulling code is (f'_x, f'_y). The difference between the error phase frequencies and the correction frequencies is responsible from this Moiré effect and creates another periodic pattern in our pupil plane at a frequency $(\frac{|f_x - f'_x|}{2}, \frac{|f_y - f'_y|}{2})$. This effect is negligible, since at the scale of the pupil plane, we just have a tiny fraction of this new period.

4.2 Simulation with perturbation

In this part, we add fake random vibration in the pupil plane before the coronagraph, that is equivalent of the DM plane.

4.2.1 Vibration simulation

Simulated vibratory perturbation can be applied on different components, such as the DM, the FPM or the Lyot Stop. Since on HiCAT the motion most likely comes from a component located before the FPM, we simulate vibrations in the DM plane.
To do so, we generate a vector of n random tip values and a vector of n random tilt values, in a certain range. We can then compute the n corresponding wavefronts in the DM plane and we add them to our phase error. After that, we can simulate the n images behind the coronagraph that are used as an input of the procedure.
We apply random vibration before summing the input images and also before applying the correction phases tested on the DM.

Except for these two extra steps, the code is applied similarly than in the previous case. We describe in the following part the results we obtain.

4.2.2 Results

As shown on Fig. 8, the vibration effect is clearly visible both before and after correction. In average, the correction is still doable, the vibration does not prevent the code from working.
The main effects of the vibration are that we can obtain random results, sometimes really good and sometimes really bad, which is due to the fact that after correction, we take a single snapshot and the random tip-tilt can
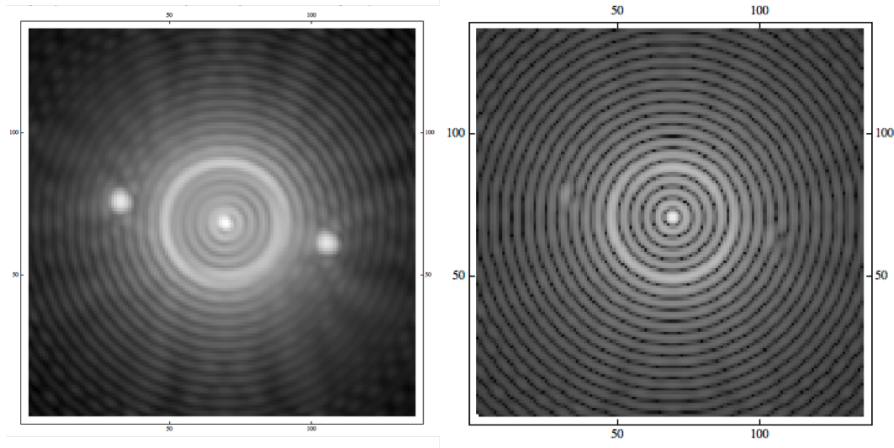
Figure 8. Coronagraphic images without and with correction, in presence of vibration. Left: Averaged image of 10 frames with random tip and tilt within the amplitude range $[-0.01\lambda, +0.01\lambda]$. Right: one single snapshot after correction, with a similar random tip-tilt vibration. In both images, the tip and tilt aberrations are visible with the asymmetry of the diffraction rings that are produced by the Lyot coronagraph. As the correction is applied at a certain position, it does not necessarily correspond to the right speckle location since a tip-tilt is added. The correction is therefore less efficient than in the case we work without vibration.
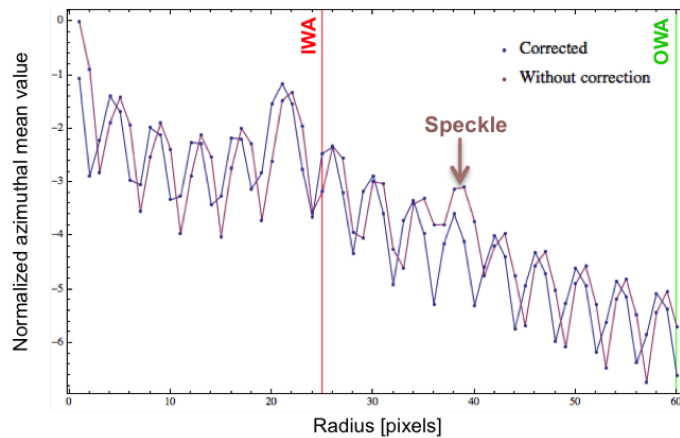

Figure 9. Azimuthal averaged intensity profiles of the simulated coronagraphic images in log scale for the noncorrected image (purple) and the corrected image (blue) that are displayed in Figure 8. The IWA and OWA of the controlled region are represented with vertical lines. A shift of the diffraction rings is observed between the two cases. The attenuation of the speckle at its location is less important than the reduction observed in the absence of vibration in Figure 7.

be small or important. Furthermore, the translation of the pattern appears on the azimuthal plot. Indeed, we observe both a translation of the rings and a smoothing of the values, as shown on Fig. 9.

The image 10 indicates the performance depending on the vibration amplitude maximum range.
For every maximum range, we apply the code 5 times and obtain a set of 5 speckle values after correction. We then look at the minimum obtained value, which corresponds to the best performance, the average value and the maximum value (worst correction). As shown on the plot 10, the higher the instability amplitude is, the more random the results are, even if in every case we can still obtain very good results (the minimum value is quite constant).
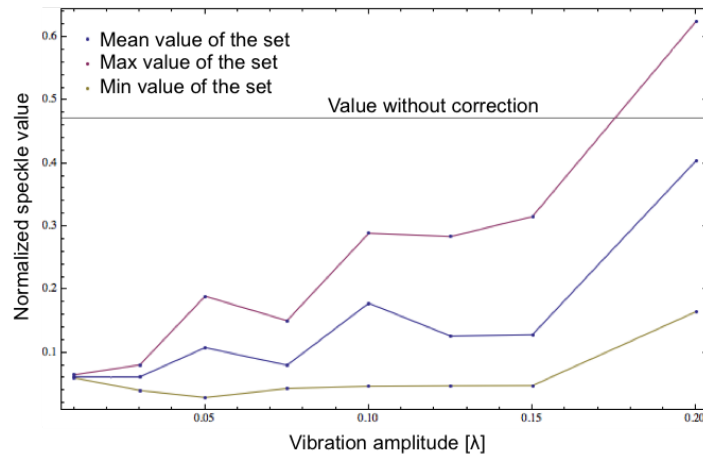
Figure 10. Intensity of the speckle after correction as a function of the maximum vibration amplitude. For every maximum range, we apply the code 5 times and obtain a set of 5 speckle values after correction. From this analysis, we retrieve the minimum obtained value, which corresponds to the best performance (yellow curve), the average value (blue curve) and the maximum value that corresponds to the worst correction (pink curve).

5. CONCLUSIONS

The HiCAT testbed will enable high-contrast imaging studies for telescopes with segmented apertures, spiders and/or central obstruction, such as WFIRST or HDST. It is designed as a coronagraph completed with two deformable mirrors to perform wavefront control and address both phase and amplitude aberrations. This year, we implemented first wavefront control codes that led us to detect an instability issue with drifts that were observed on the PSF. This issue needs to be solved to pursue our wavefront control studies. Thanks to the PSF motion analysis, we obtained strong suspects that could cause this instability. Further studies will be done thanks to an accelerometer to confirm our initial guess. In the meanwhile, a new DM mount has been designed and should provide an important improvement in terms of testbed stability.

In parallel, we coded a preliminary version of a Speckle Nulling code that gives good results in simulation mode, even in presence of pupil plane instability. Without vibration, a given speckle is fully removed after correction. In presence of vibration, we obtain a reduction of the speckle intensity in almost every case. This code will further be applied on the testbed to correct for the speckles in the chosen dark zone.

Our code will also be adapted to the case of a segmented mirror to study the effects of segments that vibrate independently on contrast performance.

REFERENCES

[1] Spergel, D., Gehrels, N., Baltay, C., Bennett, D., Breckinridge, J., Donahue, M., Dressler, A., Gaudi, B. S., Greene, T., Guyon, O., Hirata, C., Kalirai, J., Kasdin, N. J., Macintosh, B., Moos, W., Perlmutter, S., Postman, M., Rauscher, B., Rhodes, J., Wang, Y., Weinberg, D., Benford, D., Hudson, M., Jeong, W.-S., Mellier, Y., Traub, W., Yamada, T., Capak, P., Colbert, J., Masters, D., Penny, M., Savransky, D., Stern, D., Zimmerman, N., Barry, R., Bartusek, L., Carpenter, K., Cheng, E., Content, D., Dekens, F., Demers, R., Grady, K., Jackson, C., Kuan, G., Kruk, J., Melton, M., Nemati, B., Parvin, B., Poberezhskiy, I., Peddie, C., Ruffa, J., Wallace, J. K., Whipple, A., Wollack, E., and Zhao, F., "Wide-Field InfrarRed Survey Telescope-Astrophysics Focused Telescope Assets WFIRST-AFTA 2015 Report," *ArXiv e-prints* (Mar. 2015).

[2] Postman, M., Brown, T., Sembach, K., Giavalisco, M., Traub, W., Stapelfeldt, K., Calzetti, D., Oegerle, W., Michael Rich, R., Phillip Stahl, H., Tumlinson, J., Mountain, M., Soummer, R., and Hyde, T., "Advanced Technology Large-Aperture Space Telescope: science drivers and technology developments," *Optical Engineering* **51**, 011007 (Jan. 2012).

[3] Feinberg, L. D., Jones, A., Mosier, G., Rioux, N., Redding, D., and Kienlen, M., "A Cost-effective and Serviceable ATLAST 9.2m Telescope Architecture," *SPIE* **9143**, 1–11 (2014).

[4] Dalcanton, J., Seager, S., Aigrain, S., Battel, S., Brandt, N., Conroy, C., Feinberg, L., Gezari, S., Guyon, O., Harris, W., Hirata, C., Mather, J., Postman, M., Redding, D., Schiminovich, D., Stahl, H. P., and Tumlinson, J., "From Cosmic Birth to Living Earths: The Future of UVOIR Space Astronomy," *ArXiv e-prints* (July 2015).

[5] N'Diaye, M., Pueyo, L., and Soummer, R., "Apodized Pupil Lyot Coronagraphs for Arbitrary Apertures. IV. Reduced Inner Working Angle and Increased Robustness to Low-order Aberrations," *Astrophysical Journal* **799**, 225 (Feb. 2015).

[6] N'Diaye, M., Soummer, R., Pueyo, L., Carlotti, A., Stark, C. C., and Perrin, M. D., "Apodized Pupil Lyot Coronagraphs for Arbitrary Apertures. V. Hybrid Shaped Pupil Designs for Imaging Earth-like planets with Future Space Observatories," *Astrophysical Journal* **818**, 163 (Feb. 2016).

[7] Pueyo, L. and Norman, C., "High-contrast Imaging with an Arbitrary Aperture: Active Compensation of Aperture Discontinuities," *Astrophysical Journal* **769**, 102 (June 2013).

[8] Mazoyer, J., Pueyo, L., Norman, C., N'Diaye, M., and Soummer, R., "Correcting for the effects of pupil discontinuities with the ACAD method," *SPIE* **9904** (2016).

[9] Mazoyer, J., Pueyo, L., Norman, C., N'Diaye, M., van der Marel, R. P., and Soummer, R., "Active compensation of aperture discontinuities for WFIRST-AFTA: analytical and numerical comparison of propagation methods and preliminary results with a WFIRST-AFTA-like pupil," *Journal of Astronomical Telescopes, Instruments, and Systems* **2** (Mar. 2016).

[10] N'Diaye, M., Choquet, E., Pueyo, L., Elliot, E., Perrin, M., Wallace, J., Groff, T., Carlotti, A., Mawet, D., Sheckells, M., Shaklan, S., Macintosh, B., Kasdin, N. J., and Soummer, R., "High-contrast imager for Complex Aperture Telescopes (HiCAT): 1. Testbed design," in [*SPIE*], **8864** (Sept. 2013).

[11] N'Diaye, M., Choquet, E., Egron, S., Pueyo, L., Leboulleux, L., Levecq, O., Perrin, M. D., Elliot, E., Wallace, J. K., Hugot, E., Marcos, M., Ferrari, M., Long, C. A., Anderson, R., DiFelice, A., and Soummer, R., "High-contrast Imager for Complex Aperture Telescopes (HICAT): II. Design overview and first light results," in [*SPIE*], **9143**, 27 (Aug. 2014).

[12] N'Diaye, M., Mazoyer, J., Choquet, E., Pueyo, L., Perrin, M. D., Egron, S., Leboulleux, L., Levecq, O., Carlotti, A., Long, C. A., Lajoie, R., and Soummer, R., "High-contrast imager for complex aperture telescopes (HiCAT): 3. first lab results with wavefront control," in [*SPIE*], **9605**, 12 (Sept. 2015).

[13] Balasubramanian, K., Wilson, D., White, V., Muller, R., Dickie, M., Yee, K., Ruiz, R., Shaklan, S., Cady, E., Kern, B., Belikov, R., Guyon, O., and Kasdin, N. J., "High contrast internal and external coronagraph masks produced by various techniques," in [*Society of Photo-Optical Instrumentation Engineers (SPIE) Conference Series*], **8864**, 1 (Sept. 2013).

[14] Riggs, A. J. E., Kasdin, N. J., and Groff, T. D., "Recursive starlight and bias estimation for high-contrast imaging with an extended Kalman filter," *Journal of Astronomical Telescopes, Instruments, and Systems* **2**(1), 011017 (2016).

[15] Brown, R. A. and Burrows, C. J., "On the feasibility of detecting extrasolar planets by reflected starlight using the Hubble Space Telescope," *Icarus* **87**, 484–497 (Oct. 1990).

[16] Malbet, F., Yu, J. W., and Shao, M., "High-Dynamic-Range Imaging Using a Deformable Mirror for Space Coronography," **107**, 386 (Apr. 1995).

[17] Trauger, J. T., Burrows, C., Gordon, B., Green, J. J., Lowman, A. E., Moody, D., Niessner, A. F., Shi, F., and Wilson, D., "Coronagraph contrast demonstrations with the high-contrast imaging testbed," in [*Optical, Infrared, and Millimeter Space Telescopes*], Mather, J. C., ed., *SPIE* **5487**, 1330–1336 (Oct. 2004).

[18] Belikov, R., Give'on, A., Trauger, J. T., Carr, M., Kasdin, N. J., Vanderbei, R. J., Shi, F., Balasubramanian, K., and Kuhnert, A., "Toward 10 [10] contrast for terrestrial exoplanet detection: demonstration of wavefront correction in a shaped-pupil coronagraph," in [*Society of Photo-Optical Instrumentation Engineers (SPIE) Conference Series*], *SPIE* **6265**, 626518 (June 2006).

[19] Bordé, P. J. and Traub, W. A., "High-Contrast Imaging from Space: Speckle Nulling in a Low-Aberration Regime," *ApJ* **638**, 488–498 (Feb. 2006).

[20] Mazoyer, J., Baudoz, P., Galicher, R., and Rousset, G., "High-contrast imaging in polychromatic light with the self-coherent camera," *AAJ* **564**, L1 (Apr. 2014).

[21] Paul, B., Sauvage, J.-F., Mugnier, L. M., Dohlen, K., Fusco, T., and Ferrari, M., "Simultaneous phase and amplitude retrieval with COFFEE: from theory to laboratory results," in [*Ground-based and Airborne Instrumentation for Astronomy V*], *SPIE* **9147**, 91479O (July 2014).

[22] Give'on, A., Kern, B. D., and Shaklan, S., "Pair-wise, deformable mirror, image plane-based diversity electric field estimation for high contrast coronagraphy," in [*Techniques and Instrumentation for Detection of Exoplanets V*], *SPIE* **8151**, 815110 (Oct. 2011).

[23] Pueyo, L., Kay, J., Kasdin, N. J., Groff, T., McElwain, M., Give'on, A., and Belikov, R., "Optimal dark hole generation via two deformable mirrors with stroke minimization," *Appl. Opt.* **48**, 6296–6312 (Nov 2009).